




Entanglement Generation on the Double Quantum Transition of NV Ground State Via Globally Addressing Microwave Pulse

Marcel Morillas-Rozas , Alberto López-García , and Javier Cerrillo ^{*}
Área de Física Aplicada, Universidad Politécnica de Cartagena, Cartagena 30202, Spain
 (Dated: January 30, 2025)

Entanglement is a key quantum feature that enables quantum sensors to improve their sensitivity up to the Heisenberg limit. In the NV-center platform, the Heisenberg limit can only be achieved when the axes of the NV centers are parallel. Nevertheless, parallel NV centers are spectrally indistinguishable and no mechanisms to prepare entanglement in such configurations are known to date. In this work we propose for the first time a mechanism to prepare entangled states in the double quantum transition of two dipolarly coupled NV centers whose axes are parallel. Our approach is based on the NV effective Raman coupling (NV-ERC) protocol and makes use of global addressing of both NV centers with a single monochromatic microwave pulse. Supported by an adiabatic elimination analysis, several mechanisms for the preparation of different entangled states are identified which avoid participation of intermediate states in all cases, thus limiting the impact of additional unwanted noise sources. We consider the generation of different entangled states belonging to the double quantum transition, sensitive to either transverse electric fields or longitudinal magnetic fields, all with a fourfold improved sensitivity compared to conventional single NV settings.

I. INTRODUCTION

The field of quantum sensing using negatively charged nitrogen-vacancy (NV) centers in diamond [1–3] has seen a rapid growth due to the ability of NV centers to perform high-precision measurements of magnetic [4–8], electric [9, 10] and thermal fields [11, 12] with nanoscale precision [13–15]. Moreover, the ground state of the NV center shows long coherence times of the spin-1 triplet ground state [16–18], even at ambient temperatures, and they may be optically initialized and read out. Measurements can be performed extraordinarily close to the sample [19], especially in the case of nanodiamonds. These features position NV centers above some of their competitors, due to the fact that experimental NV center implementations do not require vacuum chambers or complex laser arrangements, and can be operated at room temperature.

Although the NV center ground state is a spin-1 triplet, the conventional approach is to treat it as a 2 level system by spectral selection of one of the transitions [20–33]. However, this approach requires the spectral separation between the transition used for sensing and the third level of the triplet to be significantly larger than the intensity of the control microwave (MW) pulse. If this condition is not satisfied, population leakage to the third state results in sensing limitations. Specifically, high frequency sensing and low bias magnetic field operation become unfeasible. These limitations are resolved by the NV effective Raman coupling (NV-ERC) approach [34–37], which allows to design operations that account for all three levels of the NV center without any loss of population.

One way to enhance sensing protocols is to exploit quantum entanglement, which allows to surpass the precision imposed by the standard quantum limit (SQL) and pushes it towards the Heisenberg limit. NV sensing protocols achieving a precision above the SQL have already been demonstrated [38, 39]. In particular, entanglement between a single NV center’s electronic and nuclear spins have been demonstrated [40, 41], as well as entanglement between two distant NV centers’s electronic spins mediated by dipolar interactions and addressing the transition of each NV center individually [32] by means of spectral selection. This would not be possible in the low field limit and requires a pair of NV centers that are aligned in different axes. However, the Heisenberg limit cannot be reached unless both NV centers have parallel axes. In this scenario, the NV centers become spectrally indistinguishable, precluding the use of conventional spectral selection.

Using the NV-ERC approach, we propose a protocol to overcome this limitation which allows us to generate several maximally entangled states that belong to the double quantum transition of the NV center’s ground state in a system comprising two parallel NV centers interacting via dipole interaction. The system is considered to be under the effect of an external magnetic field and is globally addressed with a single monochromatic MW field. By means of a Raman transfer, the entangled state is generated almost directly from the ground state, without participation of states that are sensitive to unwanted perturbations. All possible geometrical configurations of the two NV-centers are analyzed. An alternative approach in the limit of vanishing bias magnetic field is explored with similar efficiency. This proposal enables for the first time the creation of Heisenberg-limited sensing states for NV centers.

^{*} javier.cerrillo@upct.es

set out the two-NV-center model and establish a suitable picture for its analysis. Then, in Sec. III we present three protocols for the generation of entangled states of the double quantum transition of the two NV centers. The relevant adiabatic elimination procedure is sketched in all cases, together with an analysis of the robustness of the protocol as a function of the relevant parameters. Lastly, in Sec. IV we present some concluding remarks.

II. MODEL

The system under study consists of two NV centers $i = 1, 2$ whose axes are parallel, making them spectrally indistinguishable. Their ground state is a spin $S_i = 1$ triplet subject to the effect of a magnetic field $\mathbf{B} = (0, 0, B)^T$. The Hamiltonian describing the i -th NV center in angular units ($\hbar = 1$) reads

$$\hat{H}_{\text{NV}_i} = D\hat{S}_{i,z}^2 + \mu\mathbf{B} \cdot \mathbf{S}_i = D\hat{S}_{i,z}^2 + \mu B\hat{S}_{i,z}, \quad (1)$$

where $D/(2\pi) = 2.87$ GHz is the zero-field splitting of the electronic ground state, $\mu/(2\pi) \approx 28$ GHz/T is the gyromagnetic factor and $\mathbf{S}_i = (\hat{S}_{i,x}, \hat{S}_{i,y}, \hat{S}_{i,z})$, where $\hat{S}_{i,j}$ are the spin-1 matrices in the j -th axis of NV center i . The two NV centers are coupled via dipole-dipole interaction, whose Hamiltonian reads

$$\hat{H}_{\text{dip}} = \frac{\mu_0\mu^2}{4\pi r^3} [\mathbf{S}_1 \cdot \mathbf{S}_2 - 3(\mathbf{S}_1 \cdot \hat{\mathbf{r}})(\mathbf{S}_2 \cdot \hat{\mathbf{r}})], \quad (2)$$

where μ_0 is the vacuum permeability and $\hat{\mathbf{r}} = (\sin\theta \cos\phi, \sin\theta \sin\phi, \cos\theta)^T$ is the unit vector that points from the first NV center to the second NV center in spherical coordinates. Without any loss of generality, we consider the second NV center to be contained in the $x - z$ plane. Therefore, the unit vector in Eq. (2) becomes $\hat{\mathbf{r}} = (\sin\theta, 0, \cos\theta)^T$ in spherical coordinates, where θ is the angle with respect to $\hat{\mathbf{e}}_z$. We can expand the Hamiltonian in Eq. (2) as $\hat{H}_{\text{dip}} = \sum_{j,k} A_{jk} \hat{S}_j \otimes \hat{S}_k$, with $j, k = x, y, z$ and

$$A_{jk} = \frac{\mu_0\mu^2}{4\pi r^3} [\delta_{jk} - 3\hat{\mathbf{r}}_j \hat{\mathbf{r}}_k], \quad (3)$$

where δ_{jk} is Kronecker's delta. A direct consequence of our choice of having both NV centers in the $x - z$ plane is that all the A_{jk} coefficients that involve the coordinate y vanish except for A_{yy} . Moreover, the cross terms $A_{jk} \hat{S}_j \otimes \hat{S}_k$ with $j \neq k$ involving x and z are different from zero but may be neglected under the rotating wave approximation (RWA) after transforming our Hamiltonian into an appropriate rotating frame. Therefore, the only surviving terms in the dipole-dipole interaction Hamiltonian after applying the RWA are those of the form $A_{jj} \hat{S}_j \otimes \hat{S}_j$, with $j = x, y, z$ (see Appendix A for a detailed derivation). A_{jj} coefficients take the form $A_{jj} = \frac{\mu_0\mu^2}{4\pi r^3} (1 - 3\hat{\mathbf{r}}_j^2)$. It is worth noticing that $A_{xx} + A_{zz} = -A_{yy}$ in our setting. The two NV centers

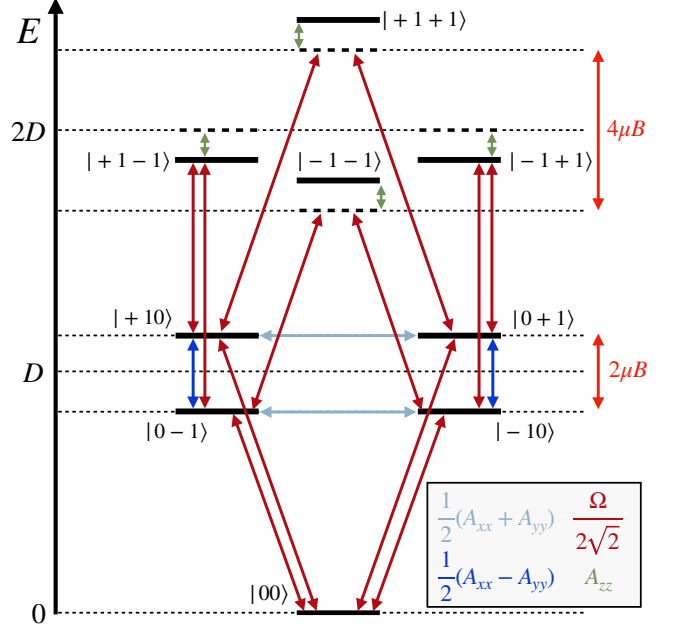


FIG. 1. Energy levels of the 2 NV center system in the canonical basis after moving to a rotating frame and performing the RWA. The wine color arrows represent the couplings due to the MW field and have a value of $\Omega/2\sqrt{2}$. The olive green arrows are shifts caused by the dipolar interactions $\hat{S}_z \otimes \hat{S}_z$ and have a value of A_{zz} . The gray and the blue arrows correspond to the couplings caused by the dipole-dipole interaction $\hat{S}_x \otimes \hat{S}_x$ and $\hat{S}_y \otimes \hat{S}_y$. They have values of $\frac{1}{2}(A_{xx} + A_{yy})$ (gray couplings) and $\frac{1}{2}(A_{xx} - A_{yy})$ (blue couplings). A_{zz} has been assumed to be positive in this figure. For the sake of simplicity, $\Delta = \omega - D$ has been set to zero in this figure.

are driven by a MW pulse of amplitude Ω and frequency ω , as shown in the Hamiltonian

$$\hat{H}_{\text{MW}} = \Omega \cos(\omega t) [\hat{S}_{1,x} + \hat{S}_{2,x}]. \quad (4)$$

Hence the full Hamiltonian of the system reads

$$\hat{H} = \hat{H}_{\text{NV}_1} + \hat{H}_{\text{NV}_2} + \hat{H}_{\text{dip}} + \hat{H}_{\text{MW}}. \quad (5)$$

To resolve its time dependence, we move to a rotating frame relative to $\hat{H}_0 = \omega (\hat{S}_{1,z}^2 + \hat{S}_{2,z}^2)$ and apply the RWA, resulting in

$$\begin{aligned} \hat{H} = & \mu B (\hat{S}_{1,z} + \hat{S}_{2,z}) - \Delta (\hat{S}_{1,z}^2 + \hat{S}_{2,z}^2) + \frac{\Omega}{2} (\hat{S}_{1,x} + \hat{S}_{2,x}) \\ & + (A_{xx} |0+\rangle\langle 0+| + A_{yy} |0-\rangle\langle 0-| + \text{H.c.}) \\ & + A_{zz} \hat{S}_{1,z} \hat{S}_{2,z}, \end{aligned} \quad (6)$$

where $|\pm\rangle = \frac{1}{\sqrt{2}}(|1\rangle \pm |-1\rangle)$ and $\Delta = \omega - D$ have been defined. The couplings are represented graphically in Fig. 1 in the canonical basis, where $\Delta = 0$ is assumed for simplicity. The complexity of the system is apparent, and the choice of a suitable basis is essential to inform the ideation of control protocols.

We propose the change to the following basis

$$|P\rangle = \frac{1}{\sqrt{2}}(|++\rangle + |--\rangle), \quad (7)$$

$$|N\rangle = \frac{1}{\sqrt{2}}(|++\rangle - |--\rangle), \quad (8)$$

$$|P_{ij}\rangle = \frac{1}{\sqrt{2}}(|ij\rangle + |ji\rangle), \quad i \neq j \quad (9)$$

$$|N_{ij}\rangle = \frac{1}{\sqrt{2}}(|ij\rangle - |ji\rangle), \quad i \neq j \quad (10)$$

where $i, j \in \{0, \pm\}$, and state $|00\rangle$ completes the basis. The couplings in this new basis are graphically depicted in Fig. 2. The Hamiltonian in the new basis contains a subspace of three states ($|N_{+-}\rangle$, $|N_{0-}\rangle$ and $|N_{0+}\rangle$) which are completely decoupled from the rest of states, i.e. it is orthogonal to the rest of the system. Therefore, unless our initial state is in this subspace, these states cannot be reached. We can split the Hamiltonian from Eq. (6) in a term for the decoupled (d) or dark subspace and one for the rest of the system, or bright subspace (b), so

$$\hat{H}' = \hat{H}_b + \hat{H}_d. \quad (11)$$

In turn, the bright subspace Hamiltonian can be expressed as the sum of three terms

$$\hat{H}_b = \hat{H}_{\text{shift}} + \hat{H}_Z + \hat{H}_{\text{MW}}, \quad (12)$$

containing the coupling and detuning shifts

$$\begin{aligned} \hat{H}_{\text{shift}} = & (A_{xx} + \Delta) |P_{0+}\rangle\langle P_{0+}| + (A_{yy} + \Delta) |P_{0-}\rangle\langle P_{0-}| \\ & + A_{zz}(|P\rangle\langle P| + |N\rangle\langle N| + |P_{+-}\rangle\langle P_{+-}|) \\ & + 2\Delta |00\rangle\langle 00|, \end{aligned} \quad (13)$$

the Zeeman splitting

$$\hat{H}_Z = \mu B (2 |P\rangle\langle P_{+-}| + |P_{0+}\rangle\langle P_{0-}| + \text{H.c.}), \quad (14)$$

and a third term for the MW driving field

$$\begin{aligned} \hat{H}_{\text{MW}} = & \frac{\Omega}{2} \left[\sqrt{2} |00\rangle\langle P_{0+}| + |N\rangle\langle P_{0+}| + |P\rangle\langle P_{0+}| \right. \\ & \left. + |P_{+-}\rangle\langle P_{0-}| + \text{H.c.} \right]. \end{aligned} \quad (15)$$

The dark subspace Hamiltonian reads

$$\begin{aligned} \hat{H}_d = & \left[\mu B |N_{0+}\rangle\langle N_{0+}| + \frac{\Omega}{2} |N_{+-}\rangle\langle N_{0-}| + \text{H.c.} \right] \\ & - (A_{xx} + \Delta) |N_{0+}\rangle\langle N_{0+}| - (A_{yy} + \Delta) |N_{0-}\rangle\langle N_{0-}| \\ & - A_{zz} |N_{+-}\rangle\langle N_{+-}|, \end{aligned} \quad (16)$$

where the first line contains the Zeeman and the MW terms, and the second and third lines contain the shifts. Note that a global Δ energy shift has been performed.

Since we the two NV centers are usually initialized in state $|00\rangle$, we may restrict our analysis to the 6-level bright subspace. Moreover, by inspecting Fig. 2(a) it

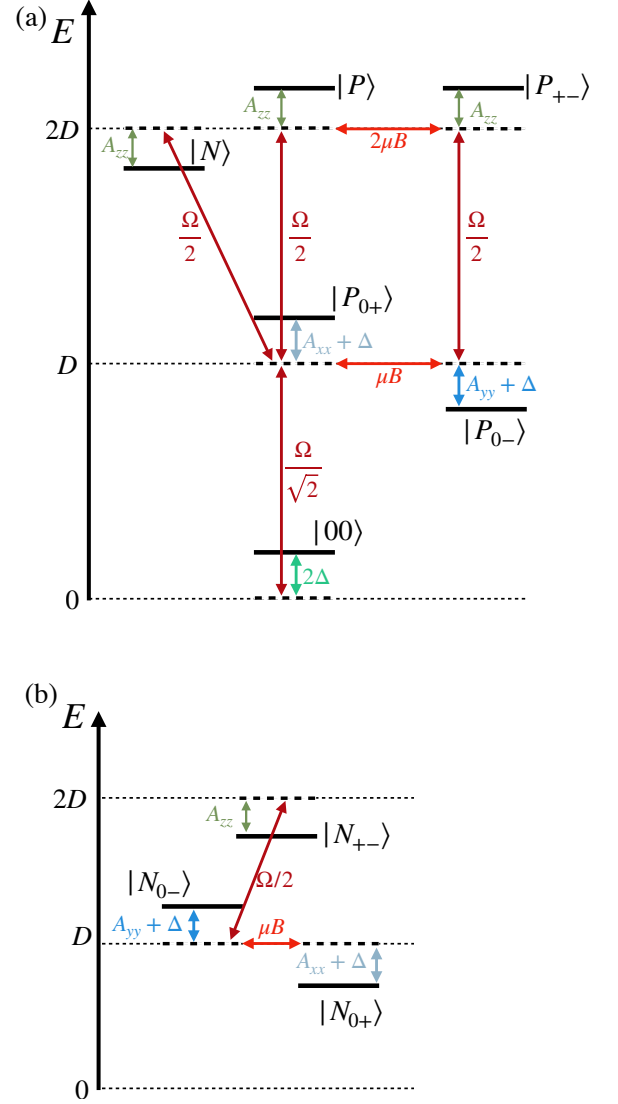


FIG. 2. Energy levels of the system of two interacting NV centers under the effect of an external magnetic field and driven by a MW pulse in the new basis. (a) contains the six states that can be reached from the ground state $|00\rangle$ (bright subspace) and (b) contains the three states that become isolated (dark subspace). In red the couplings caused by the external magnetic field, in wine color the shifts coming from the driving MW field, in olive green the shifts caused by the $\hat{S}_z \otimes \hat{S}_z$ dipole-dipole interaction, in gray the energy shifts caused by the dipole-dipole interaction $\hat{S}_x \otimes \hat{S}_x$ and the Δ detuning, in blue the energy shifts caused by the $\hat{S}_y \otimes \hat{S}_y$ interaction and the detuning and in turquoise the shift caused by the detuning Δ in the ground state.

becomes apparent that the states $|P_{+-}\rangle$ and $|P_{0-}\rangle$ can only be populated in the presence of a magnetic field. In the absence thereof, the relevant dimensionality of the system is further reduced to four levels. Among these four levels we identify two states of interest: $|N\rangle$ and $|P\rangle$ which are entangled states that belong to the double

quantum transition. In the canonical 2 NV basis, these states read

$$|N\rangle = \frac{1}{\sqrt{2}}(|+1-1\rangle + |-1+1\rangle), \quad (17)$$

$$|P\rangle = \frac{1}{\sqrt{2}}(|+1+1\rangle + |-1-1\rangle). \quad (18)$$

Note that $|N\rangle$ is insensitive to magnetic fields along the NV axes, since the first NV center accumulates a phase opposite to the second one. On the other hand, $|P\rangle$ features a fourfold increase in phase sensitivity compared to a single NV center in the single quantum transition, reaching the Heisenberg limit of measurement precision associated with the four electrons involved in the measurement. In turn, state $|N\rangle$ features a fourfold sensitivity to transverse electric fields. This makes them valuable states for sensing and we proceed to propose mechanisms for their direct production from the ground state.

III. RESULTS AND DISCUSSION

This section into three main parts, each focusing on the generation of a given entangled state belonging to the double quantum transition of the NV ground state. Subsections III A and III B make use of Raman transfer aided by $|P_{0+}\rangle$ to generate the entangled states. This is achieved by judicious combination of Ω and Δ values informed by an analysis based on adiabatic elimination of certain states from the diagram shown in Fig. 2(a). Subsection III C exploits the NV-ERC approach to generate an entangled state in zero-field conditions.

A. $|N\rangle$ state generation

By inspecting Fig. 2(a), Raman transfer between $|00\rangle$ and $|N\rangle$ aided by the state $|P_{0+}\rangle$ may be achieved when the detuning of the $|00\rangle$ and the $|N\rangle$ states is the same, i.e $2\Delta = -A_{zz}$. This tentative result ignores the effect of the remaining levels and couplings. In a more precise

analysis, adiabatic elimination of the states $|P\rangle, |P_{0-}\rangle$ and $|P_{+-}\rangle$ is used to find conditions on the values of the remaining parameters $\Omega, \mu B$ and A_{xx} that enhance the effective shift of the $|P_{0+}\rangle$, thus improving the efficiency of the transfer. To implement the adiabatic elimination the Hamiltonian in Eq. (12) is divided in four 3x3 blocks

$$\hat{H} = \begin{pmatrix} \hat{H}_1 & \hat{H}_2 \\ \hat{H}_2^\dagger & \hat{H}_3 \end{pmatrix}, \quad (19)$$

where \hat{H}_1 contains the interactions between the three states of interest ($|00\rangle, |N\rangle$ and $|P_{0+}\rangle$), \hat{H}_3 contains the interactions between the eliminated states ($|P\rangle, |P_{+-}\rangle$ and $|P_{0-}\rangle$) and \hat{H}_2 contains the interactions between the kept and the eliminated states. These 3x3 matrices read

$$\hat{H}_1 = \begin{pmatrix} 2\Delta & 0 & \Omega/\sqrt{2} \\ 0 & -A_{zz} & \Omega/2 \\ \Omega/\sqrt{2} & \Omega/2 & A_{xx} + \Delta \end{pmatrix}, \quad (20)$$

$$\hat{H}_2 = \begin{pmatrix} 0 & 0 & 0 \\ 0 & 0 & 0 \\ \Omega/2 & 0 & \mu B \end{pmatrix}, \quad (21)$$

$$\hat{H}_3 = \begin{pmatrix} A_{zz} & 2\mu B & 0 \\ 2\mu B & A_{zz} & \Omega/2 \\ 0 & \Omega/2 & A_{yy} + \Delta \end{pmatrix}, \quad (22)$$

and the effective Hamiltonian \hat{H}_{eff} resulting from adiabatic elimination is

$$\hat{H}_{\text{eff}} = \hat{H}_1 - \hat{H}_2 \hat{H}_3^{-1} \hat{H}_2^\dagger. \quad (23)$$

Due to the particular shape of \hat{H}_2 , the term $\hat{H}_2 \hat{H}_3^{-1} \hat{H}_2^\dagger$ will only cause an additional shift δ in the state $|P_{0+}\rangle$. After performing adiabatic elimination the effective Hamiltonian reads

$$\hat{H}_{\text{eff}} = \begin{pmatrix} 2\Delta & 0 & \Omega/\sqrt{2} \\ 0 & -A_{zz} & \Omega/2 \\ \Omega/\sqrt{2} & \Omega/2 & A_{xx} + \Delta + \delta \end{pmatrix}, \quad (24)$$

where

$$\delta = -\frac{(\mu B \Omega)^2 [2(A_{yy} + \Delta) - A_{zz}]}{4(A_{yy} + \Delta)(A_{zz} - 4(\mu B)^2) - A_{zz} \Omega^2} \left[\frac{2}{A_{zz}} + \frac{1}{A_{yy} + \Delta} \right] - \frac{\Omega^2}{4A_{zz}} - \frac{(\mu B)^2}{A_{yy} + \Delta}. \quad (25)$$

In the following, the conditions under which Raman transfer is most efficient are evaluated. In general, Raman transfer is achieved as long as $\Omega/2 < A_{xx} + \Delta + \delta$. An increase in δ therefore allows for larger Ω and faster transfer. Although $\Delta \approx -A_{zz}/2$ is a good first guess, Δ must be finely tuned with the expression for δ in Eq. (25), as explained in Appendix B. An example of efficient $|N\rangle$ generation is depicted in Fig. 3 which only negligibly pop-

ulates the intermediate state.

To test the transfer in other parameter configurations, the angle θ that the unit vector connecting the two NV centers forms with the z axis is considered. Since $A_{xx} \propto (1 - 3 \sin^2 \theta)$ and $A_{zz} \propto (1 - 3 \cos^2 \theta)$, it is only necessary to study the first quadrant, this is $\theta \in [0, \pi/2]$. The results are shown in Fig. 4 and illustrate that the transfer is slower as θ grows.

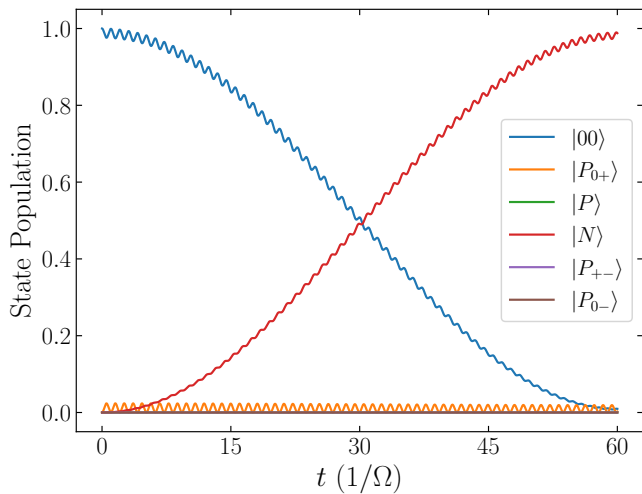


FIG. 3. Raman transfer from state $|00\rangle$ to state $|N\rangle$ aided by the intermediate state $|P_{0+}\rangle$, with $\mu B = 0.05\Omega$, $\theta = 0.426\pi$, $(\mu_0\mu^2)/(4\pi r^3) = 10\Omega$ and $\Delta = -0.49875A_{zz}$.

When $\theta = 0$ the states $|00\rangle$, $|P_{0+}\rangle$ and $|N\rangle$ are resonant, allowing Raman transfer to happen faster. As θ grows, the detuning of the intermediate state increases, which decreases the transfer rate. An interesting feature takes place at $\theta = \arccos(1/\sqrt{3})$, where the transfer is not achieved. This is because, at that specific value, $A_{zz} = 0$ and not only $|00\rangle$ and $|N\rangle$, but also $|P\rangle$ becomes resonant, making it harder to obtain a high population on $|N\rangle$ due to population leakage into $|P\rangle$. The black line in Fig. 4 indicates the time at which the maximum population in the state $|N\rangle$ is achieved for each angle. The population along this line is depicted in Fig. 5. It can be observed that for angles from $\theta = 0.334\pi$ to $\theta = \pi/2$ the transfer is much more effective. Moreover, when A_{zz} vanishes the population in state $|N\rangle$ drops significantly as a consequence of multiple resonances in the system that cause leakage to other states.

B. $|P\rangle$ state generation

In analogy to the previous case, we consider the possibility of Raman transfer from $|00\rangle$ to $|P\rangle$ via $|P_{0+}\rangle$. A tentative choice to favor this mechanism is $2\Delta = A_{zz}$. However, this case is more subtle since the state of interest $|P\rangle$ is directly coupled via the external magnetic field to one of the states we aim to eliminate.

The relevant adiabatically elimination in this case is that of the states $|P_{+-}\rangle$, $|P_{0-}\rangle$ and $|N\rangle$ and the corresponding blocks \hat{H}_1 , \hat{H}_2 and \hat{H}_3 read

$$\hat{H}_1 = \begin{pmatrix} 2\Delta & 0 & \Omega/\sqrt{2} \\ 0 & A_{zz} & \Omega/2 \\ \Omega/\sqrt{2} & \Omega/2 & A_{xx} + \Delta \end{pmatrix}, \quad (26)$$

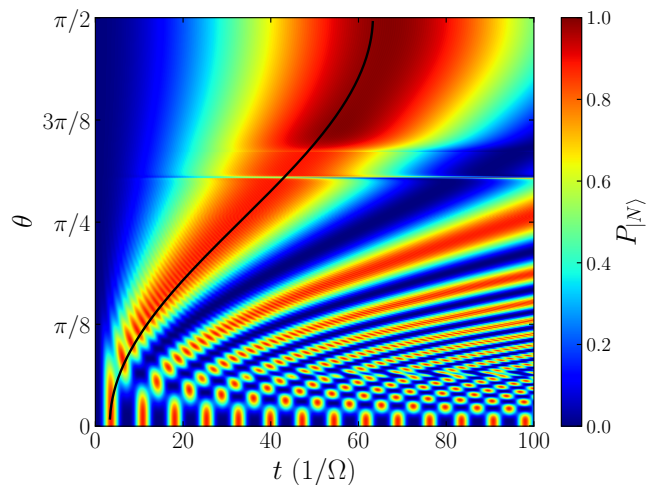


FIG. 4. Time evolution of the population in the $|N\rangle$ state for $\theta \in [0, \pi/2]$ with $\mu B = 0.05\Omega$ and $(\mu_0\mu^2)/(4\pi r^3) = 10\Omega$. The black line follows the maximum achieved population for each value of θ .

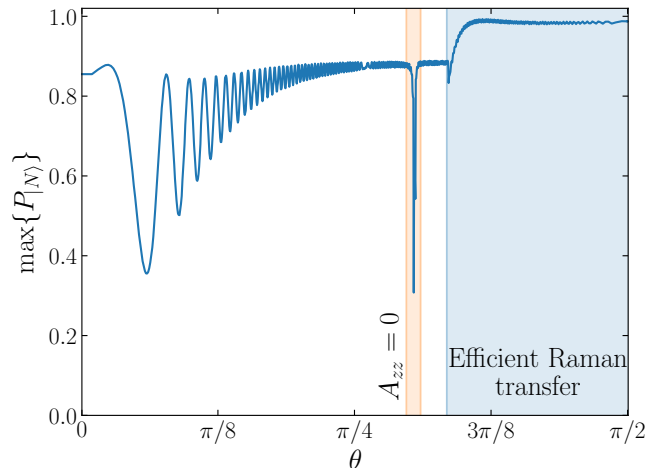


FIG. 5. Maximum population in the $|N\rangle$ state depending on the angle θ . The shaded region in orange corresponds to the region where A_{zz} vanishes and therefore the transfer is not achieved using $\mu B = 0.05\Omega$ and $(\mu_0\mu^2)/(4\pi r^3) = 10\Omega$. The blue shaded region corresponds to the angle values for which an efficient Raman transfer is achieved.

$$\hat{H}_2 = \begin{pmatrix} 0 & 0 & 0 \\ 2\mu B & 0 & 0 \\ 0 & \mu B & \Omega/2 \end{pmatrix}, \quad (27)$$

$$\hat{H}_3 = \begin{pmatrix} A_{zz} & \Omega/2 & 0 \\ \Omega/2 & A_{yy} + \Delta & 0 \\ 0 & 0 & -A_{zz} \end{pmatrix}. \quad (28)$$

In contrast with the previous case, there are more contributions in the effective Hamiltonian

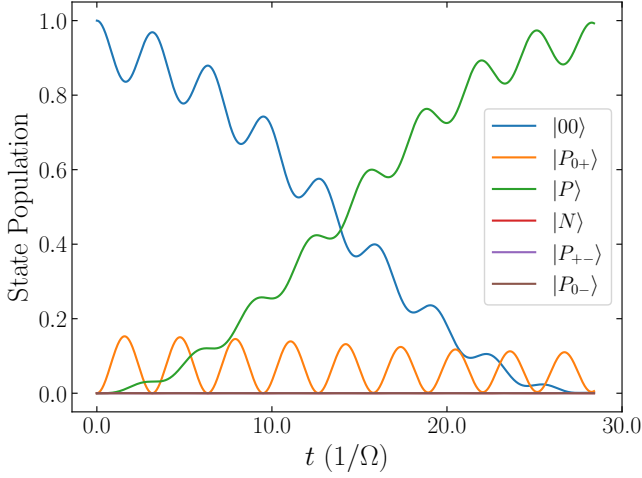


FIG. 6. Raman transfer from state $|00\rangle$ to $|P\rangle$ aided by the intermediate state $|P_{0+}\rangle$ with $\mu B = 0.001\Omega$, $\theta = 0.292\pi$, $(\mu_0\mu^2)/(4\pi r^3) = 9.09\Omega$ and $\Delta = 0.504A_{zz}$.

$$\hat{H}_{\text{eff}} = \begin{pmatrix} 2\Delta & 0 & \Omega/\sqrt{2} \\ 0 & A_{zz} + \delta' & \Omega/2 + \alpha \\ \Omega/\sqrt{2} & \Omega/2 + \alpha & A_{xx} + \Delta + \delta'' \end{pmatrix}, \quad (29)$$

where an additional coupling α between the states $|P\rangle$ and $|P_{0+}\rangle$, and additional shifts δ' and δ'' appear after the adiabatic elimination

$$\delta' = \frac{-4(\mu B)^2(A_{yy} + \Delta)}{A_{zz}(A_{yy} + \Delta) - \Omega^2/4}, \quad (30)$$

$$\alpha = \frac{(\mu B)^2\Omega}{A_{zz}(A_{yy} + \Delta) - \Omega^2/4}, \quad (31)$$

$$\delta'' = \frac{-\Omega^2}{4A_{zz}} + \frac{(\mu B)^2}{A_{yy} + \Delta - \Omega^2/4A_{zz}}. \quad (32)$$

To achieve an efficient transfer several conditions need to be satisfied. First of all, the value of α has to be very small. Moreover, the effective detuning $A_{xx} + \Delta + \delta'$ needs to be large. Lastly, the detunings from states $|00\rangle$ and $|P\rangle$ need to be very close, if not equal. In order to fulfill all these three conditions, low magnetic field B and pulse strength Ω are required. Low magnetic field is required since $|P\rangle$ and $|P_{+-}\rangle$ are coupled with $2\mu B$ and as the magnetic field grows, there is a population leakage to $|P_{+-}\rangle$ that prevents the generation of $|P\rangle$. Low pulse strength is required as per the Raman transfer condition. Therefore, the hierarchy in the parameters in this regime is $\mu B \ll \Omega < A_{zz}, A_{xx}$.

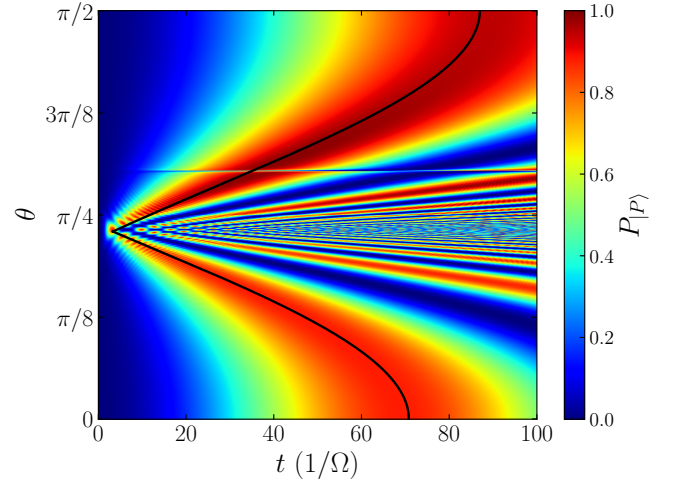


FIG. 7. Time evolution of the population in the $|P\rangle$ state for $\theta \in [0, \pi/2]$ with $\mu B = 0.001\Omega$ and $(\mu_0\mu^2)/(4\pi r^3) = 9.091\Omega$. The black line follows the maximum achieved population for each value of θ .

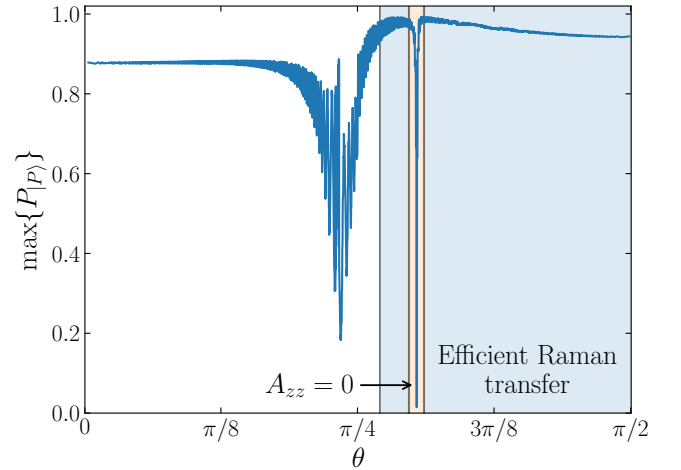


FIG. 8. Maximum population in the $|P\rangle$ state depending on the angle θ . The shaded region in blue corresponds to the region where an efficient Raman transfer is accomplished using $\mu B = 0.001\Omega$ and $(\mu_0\mu^2)/(4\pi r^3) = 9.091\Omega$. The shaded region in orange and signaled with an arrow corresponds to the region where A_{zz} vanishes and therefore the transfer is not achieved.

Having set this hierarchy, note that both α and δ' tend to 0. Therefore, $\Delta \approx A_{zz}/2$ a good condition for transfer. An instance of Raman transfer to $|P\rangle$ is shown in Fig. 6. Although the population is completely transferred from the ground state to the $|P\rangle$ state, the process is not as smooth as in the example in Fig. 3. In fact, in this case, the population in the intermediate state oscillates with a significant amplitude. This shows the importance of finely tuning the parameters. However, it is also worth noticing that in this case the entangled state $|P\rangle$ is generated much faster than $|N\rangle$, which establishes a trade-off

between the smoothness of the Raman transfer and its rate.

The transfer to the $|P\rangle$ state as a function of θ is shown in Fig. 7. As in Fig. 4 the same effect at $\theta = \arccos(1/\sqrt{3})$ appears, where A_{zz} vanishes, preventing the transfer of all the population to $|P\rangle$. For θ values between $\theta = \arcsin(1/\sqrt{3})$ and $\theta = \arccos(1/\sqrt{3})$, (the points where A_{xx} and A_{zz} vanish, respectively) we find higher frequency rates for the Raman transfer. As in the previous case, it can be observed that there is a region where the transfer achieved is much more efficient, which corresponds to angles above $\pi/4$. Fig. 8 illustrates the maximum population achieved in $|P\rangle$ as a function of θ . The transfer is very efficient for $\theta > \pi/4$, except when A_{zz} vanishes. For small values of θ the transfer is not very efficient in terms of population. However, as a consequence of being far from resonance, the maximum population reached is almost constant.

C. Zero-field entanglement generation

As it has been discussed in Sec. II, in the absence of a bias magnetic field, the dynamics of the system are reduced to a four-level system [see Fig. 2(a)], allowing to apply almost directly the NV-ERC technique [37]. By performing a change of basis to $\{|00\rangle, |P_{0+}\rangle, |++\rangle, |--\rangle\}$, the level scheme shown in Fig. 9(a) is obtained. In this setting, a maximally entangled state in the double quantum transition corresponds to an equal superposition of states $|++\rangle$ and $|--\rangle$, up to a relative phase. By adiabatically eliminating the intermediate state $|P_{0+}\rangle$, the insight gained with NV-ERC may assist in identifying parameters that achieve this goal.

The three blocks from the adiabatic elimination \hat{H}_1 , \hat{H}_2 and \hat{H}_3 and the corresponding effective Hamiltonian read

$$\hat{H}_1 = \begin{pmatrix} 0 & 0 & 0 \\ 0 & 0 & A_{zz} \\ 0 & A_{zz} & 0 \end{pmatrix}, \quad (33)$$

$$\hat{H}_2 = (\Omega/2 \ \Omega/2 \ 0)^T, \quad (34)$$

$$\hat{H}_3 = A_{xx}, \quad (35)$$

$$\hat{H}_{\text{eff}} = \begin{pmatrix} \Omega_{\text{eff}} & \Omega_{\text{eff}} & 0 \\ \Omega_{\text{eff}} & \Omega_{\text{eff}} & A_{zz} \\ 0 & A_{zz} & 0 \end{pmatrix}, \quad (36)$$

revealing an effective coupling $\Omega_{\text{eff}} = -\Omega^2/(4A_{xx})$ between states $|00\rangle$ and $|++\rangle$ [see Fig. 9(b)].

An analogy between this system and the original NV-ERC scheme can be established by mapping the NV-ERC parameters $\mu B \rightarrow A_{zz}$ and $\Omega/2 \rightarrow \Omega_{\text{eff}}$ [see Fig. 9(c)]. In contrast to NV-ERC, states $|00\rangle$ and $|++\rangle$ are shifted Ω_{eff} with respect to $|--\rangle$. However, this conserves the crucial feature of NV-ERC, which consists in the ability to fully depopulate the state $|00\rangle$ and achieve a su-

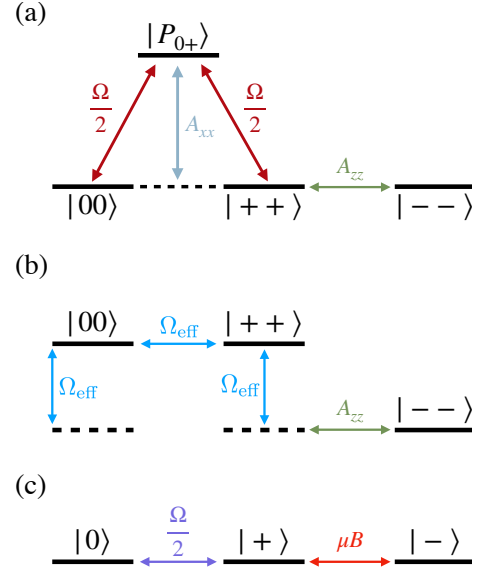


FIG. 9. (a) States of the system in zero field conditions after the change of basis. In wine red the couplings coming the MW field. In olive green the coupling coming from the $\hat{S}_z \otimes \hat{S}_z$ interactions and in gray the shift coming from the $\hat{S}_x \otimes \hat{S}_x$ interaction. (b) States after the adiabatic elimination is performed. In blue, the effective coupling. (c) NV-ERC scheme with states $|0\rangle$ and $|+\rangle$ shifted by $\Omega/2$ relative to state $|-\rangle$.

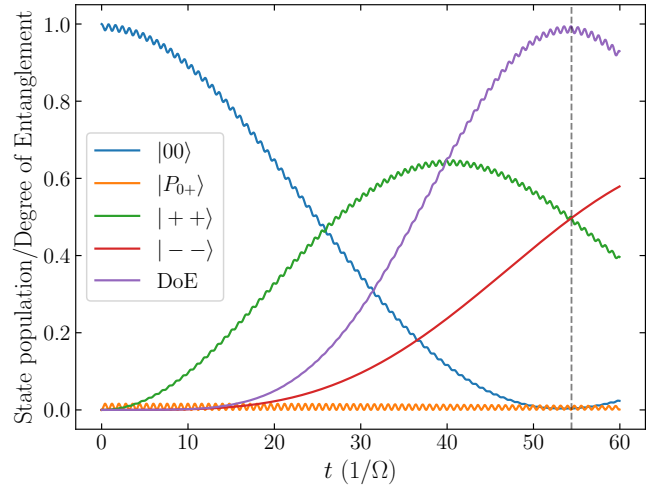


FIG. 10. Evolution of the four states in the absence of an external magnetic field. The vertical dashed line signals the time where the system reaches the maximally entangled state $|\Psi\rangle$ as the ground state becomes unpopulated. The y axis represents the population of each state and the degree of entanglement (DoE) of the evolved state which ranges from 0 for a separable state to 1 for a maximally entangled state. $\theta = 0.303\pi$, $\Omega = 40A_{zz}$, $A_{xx} = \Omega^2/(4 \times 0.1293A_{zz})$ have been used for this setup.

perposition state in the equator of the double quantum transition. We proceed to exploit this feature for the generation of an equal superposition of $|++\rangle$ and $|--\rangle$, i.e. an entangled state.

Due to the fact that NV-ERC addresses the zero-field line (i.e the MW driving frequency $\omega = D$) the detuning $\Delta = \omega - D$ vanishes. Additionally, the set of parameters that allow operation with this approach must satisfy the two regimes imposed by NV-ERC and Raman transfer, $A_{zz} < \Omega^2/4A_{xx}$ and $\Omega/2 < A_{xx}$, respectively. We find that this regime is satisfied for $\theta \simeq \arccos(1/\sqrt{3})$. Additionally, with insight from NV-ERC, we also find that $\Omega_{\text{eff}} = 1.293A_{zz}$ in the 3-level model Eq. (36) produces an equal superposition of states $|++\rangle$ and $|--\rangle$ while simultaneously depopulating state $|00\rangle$.

This prediction transfers smoothly to the full four-level Hamiltonian as illustrated in Fig. 10, where we show how, starting from the ground state $|00\rangle$, a MW pulse at frequency D produces the maximally entangled state $|\Psi\rangle \simeq \frac{1}{\sqrt{2}}(|++\rangle + e^{-i\pi/4}|--\rangle)$. This result provides evidence of the existence of an avenue of exploration for the design of alternative and increasingly optimal strategies for the generation of Heisenberg-limited sensing states for parallel NV center pairs.

IV. CONCLUSIONS

We propose a novel mechanism based on the NV-ERC approach that uses globally addressing MW pulses on two dipole-coupled parallel NV centers to prepare maximally entangled states of the double quantum transition of the NV ground state.

After simplifying the system by performing an appropriate change of basis and moving to a rotating frame, we have found the conditions that allow to generate the desired states via Raman transfer, assessed by an analysis based on adiabatic elimination. Afterwards, we have studied the behaviour of the Raman transfer with the angle θ that the two NV centers subtend, concluding that for θ values close to the resonance between the states in which we are interested, the transfer becomes faster. We have proposed an additional scheme in the case of vanishing bias magnetic field.

The generated states can serve multiple purposes, becoming sensors of transverse electric fields or longitudinal magnetic fields. Because they belong to the double quantum transition, they feature a fourfold improved sensitivity when compared to a single NV center implementation, reaching the Heisenberg limit.

ACKNOWLEDGMENTS

J.C. acknowledges support from grant PID2021-124965NB-C22 funded by MICIU/AEI/10.13039/501100011033 and by ‘‘ERDF/EU’’. M.M.R., A.L.G. and J.C. acknowledge support

from European Union project C-QuENS (Grant No. 101135359). J.C. additionally acknowledges support from grant CNS2023-144994 funded by MICIU/AEI/10.13039/501100011033 and by ‘‘ERDF/EU’’.

Appendix A: Dipole-dipole interaction Hamiltonian

In this section we derive step by step the dipole-dipole interaction Hamiltonian in Eq. (2) after transforming into the rotating frame with respect to $\hat{H}_0 = \omega (\hat{S}_{1,z}^2 + \hat{S}_{2,z}^2)$ and applying the RWA. We consider two NV centers in the $x - z$ plane, with their axes parallel, thus being spectrally indistinguishable. The two NV centers are separated a distance r and the unit vector connecting them is given by $\hat{\mathbf{r}} = (\sin\theta, 0, \cos\theta)^T$ in spherical coordinates, with $\theta =$. When expanding the products in the Hamiltonian in Eq. (2), we find that it can be expressed in the form

$$\hat{H}_{\text{dip}} = \sum_{jk} A_{jk} \hat{S}_j \otimes \hat{S}_k, \quad (\text{A1})$$

with $j, k = x, y, z$ and

$$A_{jk} = \frac{\mu_0 \mu^2}{4\pi r^3} [\delta_{jk} - 3\hat{\mathbf{r}}_j \hat{\mathbf{r}}_k], \quad (\text{A2})$$

where δ_{jk} is Kronecker’s delta. We analyze how all the different terms in the Hamiltonian read in the interaction picture separately and we apply the RWA. Note that in order to simplify the notation this derivation is performed in the $\{|+\rangle, |0\rangle, |-\rangle\}^{\otimes 2}$ basis.

- $A_{zz} \hat{S}_z \otimes \hat{S}_z$ term: Due to the fact that $[\hat{H}_0, \hat{S}_z \otimes \hat{S}_z] = 0$, after going to the interaction picture, no phase is collected by this term, leaving it unchanged.
- $A_{yk} \hat{S}_y \otimes \hat{S}_k$ and $A_{ky} \hat{S}_k \otimes \hat{S}_y$ terms with $y \neq k$: Even before going into the interaction picture these terms are 0 since $y \neq k$ and $\hat{\mathbf{r}}_y = 0$.
- $A_{xz} \hat{S}_x \otimes \hat{S}_z$ and $A_{zx} \hat{S}_z \otimes \hat{S}_x$ terms: \hat{S}_x can be rewritten as

$$\hat{S}_x = |0\rangle\langle +| + \text{H.c.}, \quad (\text{A3})$$

where $|\pm\rangle = \frac{1}{\sqrt{2}}(|1\rangle \pm |-1\rangle)$. In order to go to the interaction picture, each NV center is transformed with the unitary $\hat{U} = e^{i\omega t \hat{S}_z^2}$ as

$$\hat{U} \hat{S}_x \hat{U}^\dagger \otimes \hat{U} \hat{S}_z \hat{U}^\dagger = (e^{-i\omega t} |0\rangle\langle +| + \text{H.c.}) \otimes \hat{S}_z, \quad (\text{A4})$$

which results in \hat{S}_x collecting a phase. If this tensor product is expanded, all the terms contain temporal dependences. When RWA is applied all these terms vanish, yielding no contributions from these terms after applying the RWA.

- $A_{xx}\hat{S}_x \otimes \hat{S}_x$ term: \hat{S}_x is expressed as in Eq. (A3). Upon moving to the interaction picture, the $\hat{S}_x \otimes \hat{S}_x$ term reads

$$\begin{aligned} \hat{U}\hat{S}_x\hat{U}^\dagger \otimes \hat{U}\hat{S}_x\hat{U}^\dagger &= (e^{-i\omega t} |0\rangle\langle +| + \text{H.c.})^{\otimes 2} \\ &= e^{-2i\omega t} |00\rangle\langle ++| + |0+\rangle\langle +0| + \text{H.c.} \end{aligned} \quad (\text{A5})$$

Applying the RWA to this expression, the terms with $e^{\pm 2i\omega t}$ vanish and the remaining terms read

$$A_{xx} \left[\hat{U}(\hat{S}_x \otimes \hat{S}_x)\hat{U}^\dagger \right] \xrightarrow{\text{RWA}} A_{xx} (|0+\rangle\langle +0| + \text{H.c.}). \quad (\text{A6})$$

- $A_{yy}\hat{S}_y \otimes \hat{S}_y$ term: \hat{S}_y is expressed as

$$\hat{S}_y = i |0\rangle\langle -| + \text{H.c.} \quad (\text{A7})$$

In a similar way as with the previous term, when moving to the interaction picture, the $\hat{S}_y \otimes \hat{S}_y$ term reads

$$\begin{aligned} \hat{U}\hat{S}_y\hat{U}^\dagger \otimes \hat{U}\hat{S}_y\hat{U}^\dagger &= (ie^{-i\omega t} |0\rangle\langle +| + \text{H.c.})^{\otimes 2} \\ &= -e^{-2i\omega t} |00\rangle\langle --| + |0-\rangle\langle -0| + \text{H.c.} \end{aligned} \quad (\text{A8})$$

After performing the RWA, the terms containing $e^{\pm 2i\omega t}$ vanish and the remaining terms read

$$A_{yy} \left[\hat{U}(\hat{S}_y \otimes \hat{S}_y)\hat{U}^\dagger \right] \xrightarrow{\text{RWA}} A_{yy} (|0-\rangle\langle -0| + \text{H.c.}). \quad (\text{A9})$$

There are only contributions from the $\hat{S}_x \otimes \hat{S}_x, \hat{S}_y \otimes \hat{S}_y$ and $\hat{S}_z \otimes \hat{S}_z$ terms. If all the different contributions are added up, the dipole-dipole interaction Hamiltonian in the rotating frame after the RWA reads

$$\begin{aligned} \hat{H}_{\text{dip, RWA}} &= A_{xx} |0+\rangle\langle +0| + A_{yy} |0-\rangle\langle -0| \\ &\quad + A_{zz} |++\rangle\langle --| + \text{H.c.} \end{aligned} \quad (\text{A10})$$

Appendix B: Fine tuning of Δ

To generate the $|N\rangle$ state, starting from Eq. (24), an additional adiabatic elimination of state $|P_{0+}\rangle$ is performed, the condition to have a resonant Raman transfer reads

$$2\Delta = -A_{zz} + \frac{\Omega^2}{4(A_{xx} + \Delta + \delta)}. \quad (\text{B1})$$

When the expression for δ is substituted here, it becomes a third-degree polynomial in Δ which must be solved numerically.

In the case of the generation of the $|P\rangle$ state, performing the additional adiabatic elimination of $|P_{0+}\rangle$ in Eq.(29) yields the following resonant Raman transfer condition

$$2\Delta - \frac{\Omega^2}{2(A_{xx} + \Delta + \delta'')} = A_{zz} + \delta' - \frac{(\frac{\Omega}{2} + \alpha)^2}{A_{xx} + \Delta + \delta''}, \quad (\text{B2})$$

which again yields a third degree polynomial in Δ that has to be numerically solved after the expressions for δ', δ'' and α are substituted.

-
- [1] F. Jelezko, I. Popa, A. Gruber, C. Tietz, J. Wrachtrup, A. Nizovtsev, and S. Kilin, Single spin states in a defect center resolved by optical spectroscopy, *Applied Physics Letters* **81**, 2160 (2002).
- [2] F. Jelezko, T. Gaebel, I. Popa, A. Gruber, and J. Wrachtrup, Observation of coherent oscillations in a single electron spin, *Phys. Rev. Lett.* **92**, 076401 (2004).
- [3] M. W. Doherty, N. B. Manson, P. Delaney, F. Jelezko, J. Wrachtrup, and L. C. Hollenberg, The nitrogen-vacancy colour centre in diamond, *Physics Reports* **528**, 1 (2013), the nitrogen-vacancy colour centre in diamond.
- [4] D. Glenn, D. Bucher, J. Lee, M. D. Lukin, R. L. Walsworth, and A. Yacoby, High-resolution magnetic resonance spectroscopy using a solid-state spin sensor, *Nature* **555**, 351 (2018).
- [5] A. Ajoy, U. Bissbort, M. D. Lukin, R. L. Walsworth, and P. Cappellaro, Atomic-scale nuclear spin imaging using quantum-assisted sensors in diamond, *Phys. Rev. X* **5**, 011001 (2015).
- [6] J. L. Webb, J. D. Clement, L. Troise, S. Ahmadi, G. J. Johansen, A. Huck, and U. L. Andersen, Nanotesla sensitivity magnetic field sensing using a compact diamond nitrogen-vacancy magnetometer, *Applied Physics Letters* **114**, 231103 (2019).
- [7] H. Zheng, J. Xu, G. Z. Iwata, T. Lenz, J. Michl, B. Yavkin, K. Nakamura, H. Sumiya, T. Ohshima, J. Isoya, J. Wrachtrup, A. Wickenbrock, and D. Budker, Zero-field magnetometry based on nitrogen-vacancy ensembles in diamond, *Phys. Rev. Appl.* **11**, 064068 (2019).
- [8] C. Müller, X. Kong, J. M. Cai, K. Melentijevic, R. J. Stöhr, J. Du, M. B. Plenio, and F. Jelezko, Nuclear magnetic resonance spectroscopy with single spin sensitivity, *Nature Communications* **5**, 4703 (2014).
- [9] F. Dolde, H. Fedder, M. Doherty, T. Nöbauer, F. Rempp, G. Balasubramanian, T. Wolf, F. Reinhard, L. C. L. Hollenberg, F. Jelezko, and J. Wrachtrup, Electric-field sensing using single diamond spins, *Nature Physics* **7**, 459 (2011).
- [10] E. H. Chen, H. A. Clevenson, K. A. Johnson, L. M. Pham, D. R. Englund, P. R. Hemmer, and D. A. Braje, High-sensitivity spin-based electrometry with an ensemble of nitrogen-vacancy centers in diamond, *Phys. Rev. A* **95**, 053417 (2017).
- [11] P. Neumann, I. Jakobi, F. Dolde, C. Burk, R. Reuter,

- G. Waldherr, J. Honert, T. Wolf, A. Brunner, J. H. Shim, D. Suter, H. Sumiya, J. Isoya, and J. Wrachtrup, High-precision nanoscale temperature sensing using single defects in diamond, *Nano Letters* **13**, 2738 (2013), <https://doi.org/10.1021/nl401216y>.
- [12] Y. Y. Hui, O. Y. Chen, T. Azuma, B.-M. Chang, F.-J. Hsieh, and H.-C. Chang, All-optical thermometry with nitrogen-vacancy centers in nanodiamond-embedded polymer films, *The Journal of Physical Chemistry C* **123**, 15366 (2019).
- [13] F. Dolde, M. W. Doherty, J. Michl, I. Jakobi, B. Naydenov, S. Pezzagna, J. Meijer, P. Neumann, F. Jelezko, N. B. Manson, and J. Wrachtrup, Nanoscale detection of a single fundamental charge in ambient conditions using the NV^- center in diamond, *Phys. Rev. Lett.* **112**, 097603 (2014).
- [14] Q. Hu, K. Huang, X. Mao, G. Ran, X. He, Z. Lin, T. Hu, and S. Ran, Design of high sensitivity magnetometer based on diamond nitrogen-vacancy centers and weak signal output module, *Diamond and Related Materials*, 111858 (2024).
- [15] S. Xu, M. Liu, T. Xie, Z. Zhao, Q. Shi, P. Yu, C.-K. Duan, F. Shi, and J. Du, High-precision measurements and first-principles explanation of the temperature-dependent ^{13}C and ^{14}N hyperfine interactions of single nv^- centers in diamond at room temperature, *Phys. Rev. B* **107**, L140101 (2023).
- [16] J. V. Rakonjac, Y.-H. Chen, S. P. Horvath, and J. J. Longdell, Long spin coherence times in the ground state and in an optically excited state of $^{167}Er^{3+} : y_2sio_5$ at zero magnetic field, *Phys. Rev. B* **101**, 184430 (2020).
- [17] J. E. March, B. D. Wood, C. J. Stephen, L. D. Ferrenza, B. G. Breeze, S. Mandal, A. M. Edmonds, D. J. Twitchen, M. L. Markham, O. A. Williams, and G. W. Morley, Long spin coherence and relaxation times in nanodiamonds milled from polycrystalline ^{12}C diamond, *Phys. Rev. Appl.* **20**, 044045 (2023).
- [18] B. D. Wood, G. A. Stimpson, J. E. March, Y. N. D. Lekhai, C. J. Stephen, B. L. Green, A. C. Frangeskou, L. Ginés, S. Mandal, O. A. Williams, and G. W. Morley, Long spin coherence times of nitrogen vacancy centers in milled nanodiamonds, *Phys. Rev. B* **105**, 205401 (2022).
- [19] C. L. Degen, F. Reinhard, and P. Cappellaro, Quantum sensing, *Rev. Mod. Phys.* **89**, 035002 (2017).
- [20] A. Maudsley, Modified carr-purcell-meiboom-gill sequence for nmr fourier imaging applications, *Journal of Magnetic Resonance* (1969) **69**, 488 (1986).
- [21] A. M. Souza, G. A. Álvarez, and D. Suter, Robust dynamical decoupling for quantum computing and quantum memory, *Phys. Rev. Lett.* **106**, 240501 (2011).
- [22] Z.-Y. Wang and R.-B. Liu, Protection of quantum systems by nested dynamical decoupling, *Phys. Rev. A* **83**, 022306 (2011).
- [23] S. Kotler, N. Akerman, Y. Glickman, A. Keselman, and R. Ozeri, Single-ion quantum lock-in amplifier, *Nature* **473**, 61 (2011).
- [24] L. Cywiński, R. M. Lutchyn, C. P. Nave, and S. Das Sarma, How to enhance dephasing time in superconducting qubits, *Phys. Rev. B* **77**, 174509 (2008).
- [25] G. S. Uhrig, Keeping a quantum bit alive by optimized π -pulse sequences, *Phys. Rev. Lett.* **98**, 100504 (2007).
- [26] G. de Lange, Z. H. Wang, D. Ristè, V. V. Dobrovitski, and R. Hanson, Universal dynamical decoupling of a single solid-state spin from a spin bath, *Science* **330**, 60 (2010).
- [27] C. A. Ryan, J. S. Hodges, and D. G. Cory, Robust decoupling techniques to extend quantum coherence in diamond, *Phys. Rev. Lett.* **105**, 200402 (2010).
- [28] B. Naydenov, F. Dolde, L. T. Hall, C. Shin, H. Fedder, L. C. L. Hollenberg, F. Jelezko, and J. Wrachtrup, Dynamical decoupling of a single-electron spin at room temperature, *Phys. Rev. B* **83**, 081201 (2011).
- [29] J. Casanova, Z.-Y. Wang, J. F. Haase, and M. B. Plenio, Robust dynamical decoupling sequences for individual-nuclear-spin addressing, *Phys. Rev. A* **92**, 042304 (2015).
- [30] M. Abobeih, J. Cramer, M. Bakker, J. Zwerfer, A. Albrecht, J. Lee, F. Heremans, N. Yao, G. De Lange, and R. Hanson, One-second coherence for a single electron spin coupled to a multi-qubit nuclear-spin environment, *Nature Communications* **9**, 10.1038/s41467-018-04916-z (2018).
- [31] Z.-Y. Wang, J. E. Lang, S. Schmitt, J. Lang, J. Casanova, L. McGuinness, T. S. Monteiro, F. Jelezko, and M. B. Plenio, Randomization of pulse phases for unambiguous and robust quantum sensing, *Phys. Rev. Lett.* **122**, 200403 (2019).
- [32] T. Joas, F. Ferlemann, R. Sailer, P. J. Vetter, J. Zhang, R. S. Said, T. Teraji, S. Onoda, T. Calarco, G. Genov, M. M. Müller, and F. Jelezko, High-fidelity electron spin gates in a scalable diamond quantum register (2024), [arXiv:2406.04199 \[quant-ph\]](https://arxiv.org/abs/2406.04199).
- [33] F. Dolde, I. Jakobi, B. Naydenov, N. Zhao, S. Pezzagna, C. Trautmann, J. Meijer, P. Neumann, F. Jelezko, and J. Wrachtrup, Room-temperature entanglement between single defect spins in diamond, *Nature Physics* **9**, 139 (2013).
- [34] J. Cerrillo, S. Oviedo Casado, and J. Prior, Low field nano-nmr via three-level system control, *Phys. Rev. Lett.* **126**, 220402 (2021).
- [35] P. J. Vetter, A. Marshall, G. T. Genov, T. F. Weiss, N. Striegler, E. F. Großmann, S. Oviedo-Casado, J. Cerrillo, J. Prior, P. Neumann, and F. Jelezko, Zero- and low-field sensing with nitrogen-vacancy centers, *Phys. Rev. Appl.* **17**, 044028 (2022).
- [36] Z. Li, X. Ye, X. Kong, T. Xie, Z. Yang, P. Zhao, Y. Wang, F. Shi, and J. Du, Zero-field quantum sensing via precise geometric controls for a spin-1 system, *Phys. Rev. Appl.* **21**, 054011 (2024).
- [37] A. López-García and J. Cerrillo, Full qubit control in the nv^- ground state for low field or high frequency sensing (2024), [arXiv:2407.17461 \[quant-ph\]](https://arxiv.org/abs/2407.17461).
- [38] T. Xie, Z. Zhao, X. Kong, W. Ma, M. Wang, X. Ye, P. Yu, Z. Yang, S. Xu, P. Wang, Y. Wang, F. Shi, and J. Du, Beating the standard quantum limit under ambient conditions with solid-state spins, *Science Advances* **7**, eabg9204 (2021).
- [39] G.-Q. Liu, Y.-R. Zhang, Y.-C. Chang, J.-D. Yue, H. Fan, X.-Y. Pan, P. Li, and W. Zhao, Demonstration of entanglement-enhanced phase estimation in solid, *Nature Communications* **6**, 10.1038/ncomms7726 (2015).
- [40] R. Finsterhoelzl, W.-R. Hannes, and G. Burkard, High-fidelity entangling gates for electron and nuclear spin qubits in diamond (2024), [arXiv:2403.11553 \[quant-ph\]](https://arxiv.org/abs/2403.11553).
- [41] A. Bermudez, F. Jelezko, M. B. Plenio, and A. Retzker, Electron-mediated nuclear-spin interactions between distant nitrogen-vacancy centers, *Phys. Rev. Lett.* **107**, 150503 (2011).